

# Call for Ideas: NEO Encounter 2029

## Determination of asteroid fragmentation energy from an impactor and post-fragmentation dynamics

### Final Report

**Authors:** Patrick Michel<sup>1</sup>, Martin Jutzi<sup>2</sup>

**Affiliation:** <sup>1</sup>University of Nice-Sophia Antipolis, Côte d'Azur Observatory (France), <sup>2</sup>University of Bern (Switzerland).

**ESA Researcher:** Dario Izzo

**Date:** 22 June 2009

**Contacts:**

Patrick Michel, Côte d'Azur Observatory

Tel: +33 (0)4 92 00 30 55

Fax: +33 (0)4 92 00 30 58

e-mail: michel@oca.eu

Advanced Concepts Team, Dario Izzo

Fax: +31(0)715658018

e-mail: act@esa.int



Available on the ACT website  
<http://www.esa.int/act>

**Ariadna ID:** 08/4302  
**Study Type:** 4 months  
**Contract Number:** 20782

## I. Introduction

A question often asked when addressing the problem of the deflection of a potential impactor is: how can we make sure that the projectile will deflect and not break in large pieces the target? This is actually a fundamental problem of planetary science. The deflection of a potentially hazardous asteroid by the impact of a projectile on its surface has been studied in recent years, for instance at the European Space Agency which conducted phase-A studies of the Don Quijote mission recommended by its NEOMAP (Near-Earth Object Mission Advisory Panel) committee. While several papers addressed this concept (see e.g. Ahrens & Harris 1992, Carusi et al. 2002, Jutzi et al. 2009c), the specific impact energy threshold for catastrophic disruption (instead of cratering leading to a deflection only) was at most discussed using basic arguments in some of these papers.

The specific impact energy is defined as  $Q = 0.5 m_p v_p^2 / M_T$ , where  $m_p$ ,  $v_p$  and  $M_T$  are the mass and speed of the projectile and the target's mass, respectively; the catastrophic disruption threshold  $Q_D^*$  is defined as the specific impact energy leading to a largest fragment containing 50% of the original target's mass.

Numerical simulations of catastrophic disruptions of asteroids have shown that the impact energy required to disrupt an asteroid depends highly on its internal structure (e.g. Michel et al. 2003). The discovery of the 270 meter-size asteroid Apophis in 2004 and its non-zero probability of collision with the Earth in 2036, which depends on its passage through a keyhole during its next encounter with the Earth at less than 32,000 km in 2029 (Giorgini et al. 2008), motivates to better characterize this threshold as a function of the projectile's velocity and the internal structure of the target.

Benz and Asphaug (1999) are at the origin of the first complete investigation of the relation between  $Q_D^*$  and the target's size. The relation was derived for two impact velocities and two kinds of small body material (basalt and ice). The reason why this study is considered as the most reliable is that unlike previous efforts, it incorporated the combined effects of material strength (using a state-of-the-art brittle fragmentation model included in a Smooth Particle Hydrodynamics – SPH – code or hydrocode) and self-gravitation, thereby providing values of  $Q_D^*$  for two kinds of monolithic bodies (in basalt or ice). However, in the gravity regime, the largest fragment mass was estimated by an iterative procedure based on energy balance at the end of the simulation of fragmentation and not by simulating explicitly the gravitational phase during which reaccumulations occur and form this largest fragment. Although this procedure can give a reasonable estimate, it does not allow the characterization of the full size distribution of fragments and their ejection speeds.

The population of Near-Earth Objects is composed of bodies with a variety of spectra, and it is generally assumed that asteroids belonging to bright taxonomic classes (such as S) are rather non-porous at micro-scale, while dark-type (such as C) objects can contain a large fraction of porosity (see e.g. Britt and Consolmagno 2000). Hence, it is important to be able to model the fragmentation of both non-porous and porous bodies in order to understand this process for the different kinds of bodies that can represent members of the NEO population and to determine the catastrophic disruption threshold of such bodies as a function of impact velocities and object's sizes adapted to a deflection by a kinetic impactor.

In our study, we use an improved version of the SPH hydrocode of Benz and Asphaug (1999), which now includes a model adapted to porous materials (Jutzi et al. 2008) validated at small scales by a successful test against laboratory experiments using pumice targets (Jutzi et al. 2009a). Then, in order to explicitly characterize the fragments produced by gravitational reaccumulation in the gravity regime, we combine it with the gravitational N-body code *pkdgrav*, (Richardson et al. 2000)

as was done to reproduce asteroid families (e.g. Michel et al. 2001, 2003, Jutzi et al. 2009b). We next look for the catastrophic specific energy threshold as a function of target diameter in both the strength and gravity regime. Note that the strength regime is defined as the regime in which gravity is negligible and the main parameters influencing the impact strength of the body are its material properties, in particular the tensile strength and porosity. Targets whose size is smaller than a few hundreds of meters are in this regime. Because large targets have a higher probability of containing large incipient flaws (see Sec. III.2), it is generally found that in this regime, the impact strength decreases with the target's size. At larger sizes, gravity cannot be neglected anymore, and therefore, the impact process takes place in the gravity regime. As we will see, in this regime not only the self-gravity of the target plays a role, but also the mutual gravitational interactions of the generated fragments that are ejected influence the outcome as they can lead in some re-accumulations. Thus, in the gravity regime, the larger the target, the higher the impact strength. We will then determine in more detail in the gravity regime the outcome properties of the disruption as a function of the model used to characterize the target.

By explicitly accounting for the two main processes involved in large-scale collisions (fragmentation and gravitational interaction), our method allows us to determine not only the value of  $Q_D^*$  but also the full size and ejection velocity distributions of fragments down to the resolution limit imposed by the numerical techniques. Moreover, we can model different kinds of internal structure of the target and analyze the dependency of the value of  $Q_D^*$  and the fragments' properties on the target's properties. Here, thanks to the implementation of a model of fragmentation of porous materials, we consider two kinds of parent bodies, either porous or non-porous, which are generally believed to represent bright and dark asteroids, respectively. For a given target, the knowledge of  $Q_D^*$  as well as the outcome of the disruption can then be used as a reference to prevent that the impact conditions defined for a kinetic impactor lead to unwanted outcomes.

In the following, we present the results of our investigations, starting in Section II by a description of the two kinds of target model for which we will provide the specific impact energy threshold for disruption. The models of fragmentation are then described in Section III. Section IV summarizes the main principles of the N-body code *pkdgrav* used to follow the gravitational phase of the collision. The catastrophic disruption energy threshold of non-porous and porous targets as a function of projectile's velocity and target strengths is investigated in Section V. The outcomes in terms of fragment size and speed distributions for both models are described in Section VI and VII, respectively. Section VIII presents a comparison between these results allowing us to assess the sensitivity of the outcome properties and impact energy values upon the internal structure. Conclusions and perspectives are presented in Section IX.

## II. Models of targets

The catastrophic energy threshold and corresponding fragment properties were determined for two basic models of the target's internal structure, namely porous and non-porous.

The first model consists of a purely monolithic non-porous target that contains only a distribution of incipient flaws and no damaged zones or macroscopic voids. Its fragmentation is computed with our SPH hydrocode (Benz and Asphaug, 1994; see Sec. III.1), which includes a model of brittle failure of solid materials (see Sec. III.2) validated at small scale by comparison with laboratory experiments on basalt targets (Nakamura and Fujiwara 1991).

The second model is a porous target that consists of a body containing sub-resolution pores whose sizes are smaller than the thickness of the shock front. The fragmentation is computed using our recent model of fragmentation of porous material implemented in the SPH hydrocode (see Sec. III.3) and validated at small scale by comparison with laboratory experiments on pumice targets

(Jutzi et al. 2008, 2009a).

The values of  $Q_D^*$  have been computed using nominal values of material parameters of basalt (non-porous) and pumice (porous) targets. Then, in order to investigate the influence of the tensile and yield strengths, we computed  $Q_D^*$  for two additional kinds of targets, defined as weak non-porous and strong porous by, respectively, decreasing and increasing the tensile and yield strengths from the nominal values. Then we will investigate the outcome in terms of fragment size and speed distributions at  $Q_D^*$  using material properties of basalt for the non-porous targets and pumice for the porous ones. We believe that these two models can reasonably well represent at least two forms of asteroids or comets, usually associated with either bright (non-porous) or dark (porous) taxonomic types. Other material properties will be investigated in the future to determine whether our results can be generalized.

### **III. Numerical models of fragmentation**

#### **III.1 Numerical method**

We use a smooth particle hydrodynamics (SPH) method to simulate colliding rocky bodies from centimeter scale to hundreds of kilometers in diameter.

The equations describing an elastic solid are the usual conservation equations (mass, momentum, and energy) in which the stress tensor has a non-diagonal part, the so-called deviatoric stress tensor. With the assumption that the stress deviator rate is proportional to the strain rate, i.e., Hooke's law, and using a suitable equation of state relating the pressure to the density and internal energy, it is possible to numerically solve this set of coupled differential equations. Plasticity is introduced by suitably modifying the stresses beyond the elastic limit using a von Mises yielding relation. For the lower tensile stresses associated with brittle failure, we use a fracture model based on the nucleation of incipient flaws whose number density is given by a Weibull distribution (see Sec. III.2).

Fracture depends on the entire stress history of a given piece of material. A Lagrangian approach, in which the frame of reference is attached to the material is therefore the natural framework for solving the equations briefly described in the previous paragraph; Eulerian codes to date cannot accurately follow stress history and the development of cracks. Conventional Lagrangian codes, however, are unable to handle large material deformations, as tangling and deformation of the grid severely affect the accuracy of derivatives. Smooth particle hydrodynamics (see reviews by Benz 1990, Monaghan 1992) does not suffer from this problem. Benz and Asphaug (1994, 1995) developed a three-dimensional SPH code capable of simulating dynamical fracture of brittle material. This SPH code being an explicit code, the size of the time step is limited by the Courant condition. In practice, this means that the time step cannot exceed a fraction of the time needed by an elastic wave to cross a resolution element. If this element is of size  $h$ , numerical stability requires that  $dt < h=c$ , where  $c$  is the wave speed.

Details of the SPH method can be found in the paper by Benz (1990). A description of how the equations for solving our problems are cast in the SPH framework is exposed in Benz and Asphaug (1994, 1995).

#### **III.2 Classical model of brittle failure**

The most commonly used fracture model is derived from a continuum model of fragmentation developed by Grady and Kipp (1980). It is based on the assumption that a brittle solid contains an initial distribution of incipient flaws, supposed to be represented by a Weibull distribution (Weibull

1939). This is a probability distribution that represents the most likely number of flaws per unit volume having failure strains lower than  $\epsilon$  by the power law:

$$n(\epsilon) = k \epsilon^m,$$

where  $k$  and  $m$  are material constants called the Weibull coefficients. These parameters have been measured for a number of geological and industrial materials, including basalt (Nakamura et al. 2007), although data are still scarce for some important rocks that may well represent asteroids. Cracks evolve in a solid when Weibull flaws activate, i.e. when their failure strain is exceeded, and grow at some fraction of the sound speed. Grady and Kipp model local stress release due to the growth of cracks with a state variable  $D$  (for "damage") that goes from 0 to 1, and which is derived from the Weibull distribution and strain history. Damage expresses the reduction in strength under tensile loading. The reduction in stress is expressed as:

$$\sigma_D = \sigma (1 - D)$$

where  $\sigma$  is the elastic stress in the absence of damage and  $\sigma_D$  is the damage-relieved stress. A material with sufficient cracks to have a damage  $D=0.5$  feels half the stress it would otherwise feel under the same tensile strain. A fully damaged material feels no tensile stress whatsoever, and thus such material would be considered as a fully damaged cohesionless body, explaining why we do not need such a model to address the disruption of cohesionless bodies. In more than one dimension, the equation above is replaced by the following relationship between the stress tensor  $\sigma_{ij}$  and the strain tensor  $\epsilon_{ij}$ :

$$\sigma_{ij} = -P^* \delta_{ij} + (1-D) S_{ij},$$

where  $P^* = P$  if  $P > 0$  ( $P$  being the pressure) or  $P^* = (1-D) P$  if  $P < 0$  and  $S_{ij}$  is the deviatoric stress tensor (non-diagonal part).

In the Grady-Kipp model, damage is a state variable: it is equal to the fractional volume that is relieved of stress by the network of growing cracks. The Weibull distribution being a number density, damage is best viewed as a dimensionless volume density. A crack relieves stresses in a neighborhood approximately equal to a circumscribed sphere (Walsh 1965), such that damage in a volume  $V$  with a single crack in it of half length  $a$  is:

$$D = (4 \pi a^3) / (3 V).$$

Grady and Kipp assume that cracks grow at a constant velocity  $c_g$ , so that the half-length of a growing crack is:

$$a = c_g (t-t'),$$

where  $t'$  is the crack activation time. The crack growth speed is a fraction of the speed of a longitudinal elastic wave (Lawn and Wilshaw 1975), generally assumed to be about 0.4. If the damaged volume is a sphere of radius  $R_s$  and a single crack is propagating in it, then the differential form for the cube root of damage is expressed as:

$$d D^{1/3} / dt = c_g / R_s.$$

Under an increasing strain, increasing numbers of Weibull flaws activate in succession, with different crack lengths. Damage becomes an integral over all these growing cracks. Grady and Kipp approximate this integral with the differential equation:

$$d D^{1/3} / dt = [ (m+3) \alpha^{1/3} \varepsilon^{m/3} ]/3,$$

where

$$\alpha = 8 \pi c_g^3 k / [(m+1)(m+2)(m+3)]$$

which allows damage to grow monotonically in a realistic manner when strain rate varies with time. By solving stress as a function of time and setting its derivative to zero, Grady and Kipp derive the dynamic tensile strength of a material:

$$\sigma_T = [3E (m+3) d\varepsilon/dt] / [(m+3)(m+4)^{-(m+4)/(m+3)} \alpha^{-1/(m+3)}]$$

where E is the elastic modulus of the undamaged material. If  $d\varepsilon/dt \rightarrow 0$  the material becomes strengthless. This reflects the fact that theirs is a dynamical model and should only be applied at high loading rates; in practice, one takes  $\sigma_T$  to be the maximum of the value given by the expression above and the static strength.

To compute the evolution of the damage propagation as a result of a stress increase in a solid body, the equations to be solved are the well-known conservation equations of hydrodynamics and can be found in standard textbooks. Then, a basic Hooke's law model is assumed in which the stress deviator rate is proportional to the strain rate. Provided that an equation of state links the pressure to the density and internal energy, this set of equations can be solved and describes a perfectly elastic material. Then, the plastic behavior, which represents the fact that a critical stress always exists that results in permanent deformation, can be introduced in the equations. Generally, a von Mises criterion is used to limit the deviatoric stress tensor. Then the fracture model described above is used to compute the crack propagation.

### III.3 Model including porosity

While porosity at large scales can be modeled explicitly by introducing macroscopic voids, porosity on a scale much smaller than the numerical resolution and the thickness of the shock front has to be modeled through a different approach. Our porosity model is based on the *P-alpha* model originally proposed by Herrmann (1969) and later modified by Carroll and Holt (1972). The model provides a description of microscopic porosity with pore-sizes beneath the spatial resolution of our numerical scheme (sub-resolution porosity) and which is homogeneous and isotropic.

The basic idea underlying the *P-alpha* model consists of separating the volume change in a porous material into two parts: the pore collapse on one hand and the compression of the material composing the matrix on the other hand. This separation can be achieved by introducing the so-called distention parameter  $\alpha$  defined as :

$$\alpha \equiv \rho_s / \rho, \quad (1)$$

where  $\rho$  is the bulk density of the porous material and  $\rho_s$  is the density of the corresponding solid (matrix) material. Porosity is defined as the total of all void space within a rock; as a function of distention, it is defined as  $1 - 1/\alpha$ . According to its definition, the distention varies in the range  $\alpha_0 > \alpha > 1$ , where  $\alpha_0$  is the initial distention. Using the distention parameter  $\alpha$ , the equation of state (EOS) can be written in the general form:

$$P = P(\rho, U, \alpha). \quad (2)$$

According to [Carroll and Holt \(1972\)](#), the EOS of a porous material can explicitly be written as

$$P = 1/\alpha P_s(\rho_s, U_s) = 1/\alpha P_s(\alpha\rho, U), \quad (3)$$

where  $P_s(\rho_s, U_s)$  represents the EOS of the solid phase of the material (the matrix). A crucial assumption in this model is that the pressure depends on the density of the matrix material. The pore space is modeled as empty voids and the internal energy  $U$  is assumed to be the same in the porous and the solid material ( $U = U_s$ ), which implies that the surface energy of the pores is neglected. The factor  $1/\alpha$  in Eq. (3) was introduced by [Carroll and Holt \(1972\)](#) to take into account that the volume average of the stress in the matrix is given by:

$$P_s = \alpha P, \quad (4)$$

where  $P$  is the applied pressure.

In the *P-alpha* model, the distention is solely a function of the pressure  $P$ :

$$\alpha = \alpha(P) \quad (5)$$

where  $P = P(\rho, U, \alpha)$ . The relation between distention and pressure is often divided in an elastic regime ( $P < P_e$ ) and a plastic regime ( $P > P_e$ ), where  $P_e$  is the pressure at which the transition between the two regimes occurs. Analytical expressions used for these relations are indicated in [Jutzi et al. \(2008\)](#). More realistic relations can be obtained experimentally by means of a one dimensional static compression of a sample, during which the actual distention  $\alpha_m$  is measured as a function of the applied pressure  $P_m$ . The resulting crush-curve  $\alpha_m(P_m)$  then provides the required relation between distention and pressure for the material.

The time evolution of the distention parameter can be written as

$$d\alpha/dt = d\alpha/dP \cdot dP/dt$$

Eq. (3) associated with a crush-curve defines the constitutive equation that describes the compaction behavior of a porous material. In the original work of [Herrmann \(1969\)](#) and [Carroll and Holt \(1972\)](#), the *P-alpha* model was intended to be a first order theory in which shear strength effects are considered secondary and consequently, the stress tensor was assumed to be diagonal. In this work, we use the full stress tensor and therefore, we extend the original model with a relation between the distention and the deviatoric stress tensor. Details can be found in [Jutzi et al. \(2008\)](#).

The difference in impact response of either a porous or a non-porous body is well demonstrated on Fig. 1, which shows two snapshots of the disruptions of the two kinds of parent bodies using the same impact conditions. One can see that the porous body experiences compaction.

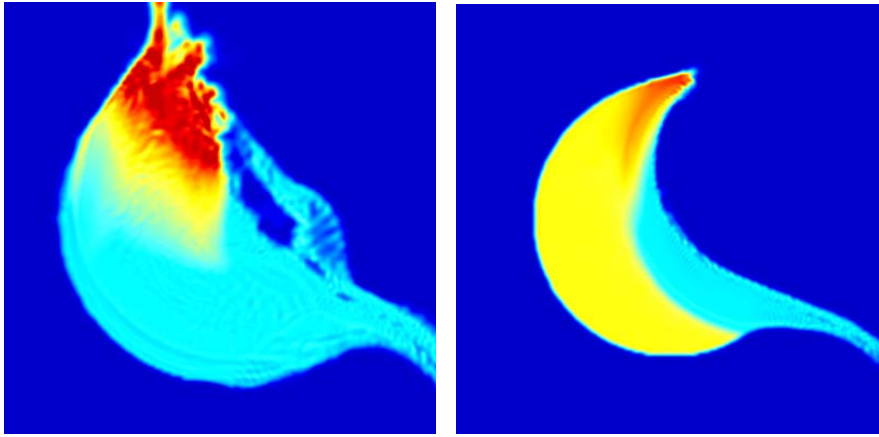


Figure 1: 2D Snapshots of 3D SPH simulations of catastrophic disruption using the same impact conditions at time  $t = 100$  s after the impact. Left: non-porous parent body; right: porous parent body. The colors correspond to the magnitude of the velocity, from light blue to red (light blue: negative velocity, red: positive velocity).

#### IV. The N-body code

The simulations of the gravitational phase of a catastrophic disruption are carried out using *pkdgrav*, a numerical gravity solver first developed for cosmological modeling at the University of Washington (Stadel 2001). The code was adapted to treat hard-sphere collisions for planetesimal modeling (Richardson et al. 2000). The main technical features of the code include a hierarchical tree algorithm for reducing the computational cost of interparticle force calculations and a complete parallel implementation for balancing work across an arbitrary number of processors. These features place *pkdgrav* among only a handful of truly parallel treecodes available to the astronomy/planetary science community for modeling complex systems of gravitationally and collisionally interacting particles. Many aspects of the code, including the ability to model semi-rigid bodies, are, as far as we know, unique to *pkdgrav*. This section provides some details of the numerical method used in *pkdgrav* relevant to the proposed work.

##### IV.1. Equations of Motion

Fundamentally, *pkdgrav* solves Newton's equations of motion for self-gravitating point particles:

$$\ddot{\mathbf{r}}_i = - \sum_{j \neq i} \frac{G m_j (\mathbf{r}_i - \mathbf{r}_j)}{|\mathbf{r}_i - \mathbf{r}_j|^3},$$

where  $\mathbf{r}$  denotes position (in three spatial dimensions),  $m$  is mass,  $G$  is the gravitational constant,  $i, j \in [1, N]$  are indices,  $N$  is the number of particles, and the derivatives are with respect to time. Note that in the absence of time-saving measures such as the treecode, computation of interparticle forces scales as  $\frac{1}{2}N(N-1)$  (the  $\frac{1}{2}$  comes from Newton's Third Law which states that the acceleration on particle  $i$  due to  $j$  is equal and opposite of that on  $j$  due to  $i$ , saving half the computations)<sup>1</sup>. These

<sup>1</sup> With the treecode, the potentials due to distant groups of particles are approximated by multipole expansions about the group centers of mass, resulting in computation times that scale as  $\mathcal{O}(N \log N)$  but that give rise to small force errors (c.f. Barnes and Hut 1986). The errors are controlled by a single parameter that determines how small and distant a group of particles must be to use the approximation. Typical implementations expand the potentials to quadrupole order; *pkdgrav* expands to hexadecapole order.

differential equations are solved using a second-order “leapfrog” integrator:

$$\begin{aligned} \dot{r}_{i,n+1/2} &= \dot{r}_{i,n} + (h/2)\ddot{r}_{i,n} && \text{"kick"} \\ r_{i,n+1} &= r_{i,n} + h\dot{r}_{i,n+1/2} && \text{"drift"} \\ \dot{r}_{i,n+1} &= \dot{r}_{i,n+1/2} + (h/2)\ddot{r}_{i,n+1} && \text{"kick"}, \end{aligned}$$

where  $h$  is the (constant) timestep that takes the system from step  $n$  to step  $n+1$ . Each stage in the kick-drift-kick sequence is performed for all particles  $i$ . The timestep  $h$  is chosen to ensure adequate sampling of the shortest dynamical time in the system, which is typically  $\approx 1/\sqrt{G\rho}$ , where  $\rho$  is the characteristic mass density of a particle. The principal advantage of the leapfrog method, which as shown “kicks” the particle velocities while holding the positions constant, then “drifts” the particle positions while holding the velocities constant, is that it is symplectic, meaning it has good conservation properties for sufficiently small  $h$  (see Saha and Tremaine 1992 for details). Another advantage is that it makes collision detection particularly simple (next section). In the leapfrog scheme, the accelerations  $\ddot{r}_i$  are computed using the treecode after each drift (and at the very start of the simulation), before the next kick.

## IV.2 Collision Handling

For the purpose of modeling collisions between particles, each particle is treated as a rigid sphere of radius  $R_i$ . Since particle positions change only during the drift step, and the change is linear in time, collisions between particles can be predicted by solving a quadratic equation for the time of surface contact between any two approaching spheres (Richardson et al. 2000). (This is an approximation since in reality the particles generally do not move through the intervening space in straight lines, but it is consistent with the order of the integration.) To reduce the cost of the collision search, a variant of the *pkdgrav* tree algorithm is used to find the  $N_n$  closest neighbors of each particle (the method scales as  $N_n \log N$ ). Typically  $N_n \approx 32$ , which allows for the possibility of detecting collisions with distant neighbors approaching at faster relative speeds than the closest neighbors.

A collision search is performed for all particles at the beginning of the drift step and any potential collisions found are processed in time order. Once a collision is detected, the outcome is determined based on user-defined parameters that include the amount of dissipation (restitution and surface friction) and whether particles merge or bounce on contact. Particles that merge result in the formation of a sphere whose mass is the sum of the masses of the original particles, and whose position and velocity are those of the center of mass of those particles. This happens when the relative speed between particles is smaller than a fraction of the mutual escape speed. Otherwise, they bounce. For bouncing, the usual billiard ball restitution equations are used (including spin if there is surface friction; c.f. Richardson 1994). The values of the coefficients of restitution are poorly constrained; we chose to set the normal coefficient of restitution to 0.3 for porous targets and 0.5 for non-porous ones, and the tangential coefficient to 1 (representing no surface friction). Michel et al. (2002) already found that values of the normal coefficient of restitution in the range 0.5-0.8 led to similar outcomes for non-porous bodies, and we checked that the same holds true in the case of porous bodies for values in the range 0.3-0.5. After a collision, the particles involved (and any particles in the system that were identified as possibly colliding with either of them later in the drift interval) are subject to a new potential collider search. In this way, all collisions are detected and processed in the correct time order, even if a given particle suffers more than one collision in a drift interval. Once all collisions have been handled, the final end-of-drift particle positions are assigned and the interparticle gravity is computed.

The gravitational phase is thus computed using this N-body code. Initial conditions are starting the

fragment positions and velocities resulting from the fragmentation phase computed by the SPH hydrocode. The N-body simulations thus provide the final outcome properties of fragments of a large-scale disruption (the size, position, ejection velocity of each of fragments), which can be directly plotted as size and ejection velocity distributions (see Sec. VI to VIII).

## V. Catastrophic disruption threshold

In this section, we reproduce the text of a paper submitted to the journal *Icarus* describing the results of our investigation, explicitly acknowledging support from the Ariadna program and ACT Team of ESA. A part of this study, specifically devoted to bodies of 300 m-size (same order of Aphophis' size) has been published in the proceedings of the Planetary Defense Conference that took place in Grenada (Spain) in April 2009 (Michel et al. 2009), explicitly acknowledging the support from the Ariadna program and ACT team of ESA.

To characterize  $Q_D^*$  for a given impact speed, we have proceeded by trial and errors, by making several simulations and then looking for those that led to a largest fragment containing 50% of the parent body's mass. We used about  $2 \times 10^5$  SPH particles to perform the simulations. In the gravity regime, in a first step, we computed explicitly the fragmentation phase by using the SPH hydrocode. We obtained a first estimate of the largest fragment mass by using the iterative procedure based on energy balance developed by Benz and Asphaug (1999). Once the impact conditions expected to lead to the appropriate remnant mass were identified, the complete simulation was carried out, this time including both the fragmentation and gravitational phases. The gravitational phase was computed using a stepsize of 50 s (several runs were made with a stepsize of 5 s and obtained similar results) and was carried out to a simulated time of 11.6 days after which the outcome does not change anymore. Note that the mass of the largest remnant found by the complete simulation (including the gravitational phase) is in a good agreement with the mass found by the iterative energy balance method (the difference is typically of the order 3-5 %).

### V.1. Catastrophic impact energy threshold as a function of target diameter for non-porous and porous materials

Table 1 gives the nominal material properties of basalt and pumice used in our two models of internal structure (non-porous and porous). We define them as nominal, because in order to characterize the influence of the tensile and shear strengths, we will modify the values of these parameters to compute  $Q_D^*$  in the following subsection. Table 2 gives the impact conditions of our simulations (which, in the gravity regime, include the explicit computation of the gravitational phase) for all the investigated diameters and for the two nominal models. Note that the largest fragment from these simulations does not contain exactly 50% of the target's mass since it would be computationally unreasonable to look for the impact conditions that lead to the exact value. To determine  $Q_D^*$ , we performed at least one additional impact simulation around the specific energy threshold and we interpolated through the corresponding values of the impact energy to derive the exact value of  $Q_D^*$ . Note that in the gravity regime, we used the mass of the largest remnant obtained by the energy balance method to perform the interpolation. In all simulations presented here, we obtained  $0.35 < M_{lr}/M_{pb} < 0.65$ , where  $M_{lr}$  and  $M_{pb}$  are the largest remnant and parent body masses, respectively.

	Nominal Non-Porous	Nominal Porous
m	9.5	9.5
k	$3.0 \times 10^{28}$	$8.0 \times 10^{37}$
Y	$3.5 \times 10^{10}$	$3.5 \times 10^{10}$
$\sigma_T(3 \text{ cm})$	$3.2 \times 10^8$	$3.2 \times 10^7$

Table 1: Nominal material properties of non-porous and porous targets.  $m$  and  $k$  (in  $\text{cm}^{-3}$ ) are the Weibull parameters used to characterize the distribution of incipient flaws.  $Y$  (in  $\text{dynes/cm}^2$ ) is the yield strength, and  $\sigma_T(3\text{cm})$  is the (size dependent) tensile strength (in  $\text{dynes/cm}^2$ ) of a 3 cm-diameter target.

$R_t$ (km)	Type	$R_p$ (km)	$Q$ ( $\text{erg g}^{-1}$ )	$M_{lr}/M_{pb}$
0.00003	NP	0.0000022	$1.79 \times 10^7$	0.49
0.003	NP	0.00013	$3.34 \times 10^6$	0.51
0.3	NP	0.01	$1.63 \times 10^6$	0.54
1.0	NP	0.058	$8.38 \times 10^6$	0.54
10.0	NP	1.59	$1.80 \times 10^8$	0.46
100.0	NP	41	$3.10 \times 10^9$	0.50
0.00003	P	0.0000024	$4.74 \times 10^7$	0.50
0.003	P	0.00011	$4.49 \times 10^6$	0.63
0.3	P	0.0093	$2.50 \times 10^6$	0.51
1.0	P	0.045	$8.04 \times 10^6$	0.49
10.0	P	1.01	$9.55 \times 10^7$	0.56
100.0	P	27.3	$1.90 \times 10^9$	0.48

Table 2: Summary of simulation parameters. NP and P refer to our nominal Non-Porous and Porous targets, respectively (see Table 1). The projectile's angle of incidence is  $45^\circ$  and the impact speed is 3 km/s. Impact conditions are defined by the specific impact energy  $Q = (\text{projectile kinetic energy})/(\text{target mass})$ , which involves the projectile's radius  $R_p$ .  $M_{lr}/M_{pb}$  is the resulting mass ratio of the largest remnant to the parent body. All simulations are aimed at being close to the catastrophic disruption threshold defined as  $M_{lr}/M_{pb} = 0.5$ . Note that for targets with a radius  $R_t \geq 0.3$  km, the gravitational reaccumulation was explicitly simulated.

Figure 2 presents the relationship between  $Q_D^*$  and target diameter for the two kinds of parent bodies and for a projectile speed of 3 km/s and impact angle of  $45^\circ$ . The material properties of the porous target are those that provided the best match to the impact experiments on pumice targets (Jutzi et al. 2009a). Non-porous targets are characterized by material properties of basalt (Benz and Asphaug 1994), so in this case our simulations, using an improved version of the SPH hydrocode, revisit the values of  $Q_D^*$  estimated by Benz and Asphaug (1999), who used similar targets. As expected, in the strength regime, the value of  $Q_D^*$  decreases with target diameter, while in the gravity regime,  $Q_D^*$  increases with target diameter due to the gravitational attraction that has to be overcome and that increases with the size of the target. However, in the strength regime (radius smaller than a few hundreds meters), porous targets are stronger than non-porous ones, as more energy is required to disrupt them (as found in laboratory experiments). The opposite is true in the gravity regime, where the porous targets become weaker than non-porous ones. To explain this change of impact response we first point out that in the strength regime, the largest remnant is one large intact fragment while in the gravity regime, targets are first totally shattered by the fragmentation before building up the largest remnant through gravitational reaccumulation. One reason for the change in impact response is therefore linked to the fact that the target density of the porous target is smaller than that of non-porous targets, leading to a less efficient reaccumulation in the porous case. We use a bulk density of  $1.3 \text{ g/cm}^3$  for porous targets, and  $2.7 \text{ g/cm}^3$  for non-porous ones, in order to be consistent with the estimated densities of dark-type and bright-type asteroids (e.g. Yeomans et al. 1997, Wilkison et al. 2002). Therefore, target's masses are different for the two kinds of bodies at a given diameter. Figure 3 shows the relation between  $Q_D^*$  and mass. Compared to the relation involving sizes, the difference is not huge, but the curve for porous bodies in the gravity regime is indeed shifted toward the one for non-porous bodies. Note that the bulk

density of the projectiles impacting both kinds of targets is set to  $2.7 \text{ g/cm}^3$ . We checked in a few cases that using a projectile with a bulk density of  $1.3 \text{ g/cm}^3$  does not lead to significantly different results than those obtained with a higher density. Another reason for the change of impact response in the gravity regime is related to the shear strength that is generally higher in non-porous targets than in porous ones. Note that while the value of the yield strength ( $Y$ ) corresponds to the shear strength in non-porous materials, this is not the case in our porous material. As described in Jutzi et al. (2008),  $Y$  is the yield strength of the matrix material and does not correspond to the "bulk" shear strength of the porous material (which is generally lower). As Leinhardt and Stewart (2008) showed, the shock wave decays more rapidly in strong (high shear strength) materials than in weak (low shear strength) materials. The authors conclude that the stronger the material, the more energy is partitioned into overcoming the shear strength. Since our porous material has a much smaller bulk shear strength than the non-porous material, more energy is partitioned into plastic deformation in the latter case. This effect could, at least partially, compensate the effect of the dissipation of energy by compression ( $PdV$  work, where  $P$  is the pressure and  $V$  is the volume) in porous targets. In section IV.5 we investigate  $Q_D^*$  for different values of the shear strength. We find that in the gravity regime,  $Q_D^*$  for non-porous targets decreases significantly with decreasing shear strength which is not the case for porous targets. The influence of the shear strength is less strong for smaller targets (in the strength regime) since in this regime, the tensile strength dominates the outcome (size of intact fragments) and, in addition, the impact energies are lower and the resulting shock waves are less strong. We will investigate the fraction of the incoming energy that goes into dissipation by compaction, plastic deformation or kinetic energy of the target in a further study.

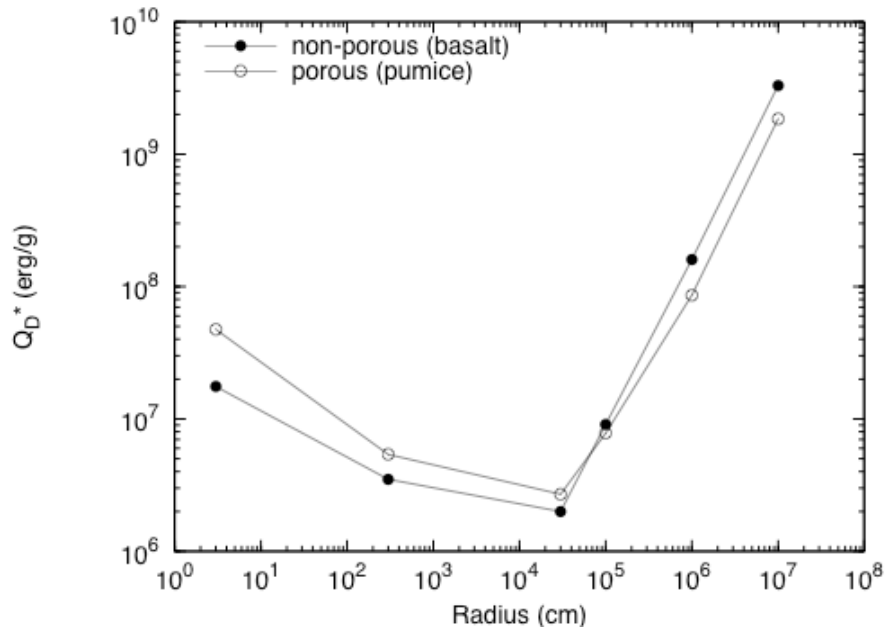


Figure 2: Catastrophic specific impact energy threshold  $Q_D^*$  (erg/g) as a function of the target radius  $R$  (cm). The impact speed and angle are  $3 \text{ km/s}$  and  $45^\circ$ , respectively. The internal structure of the target is either porous or non-porous, as indicated on the plot.

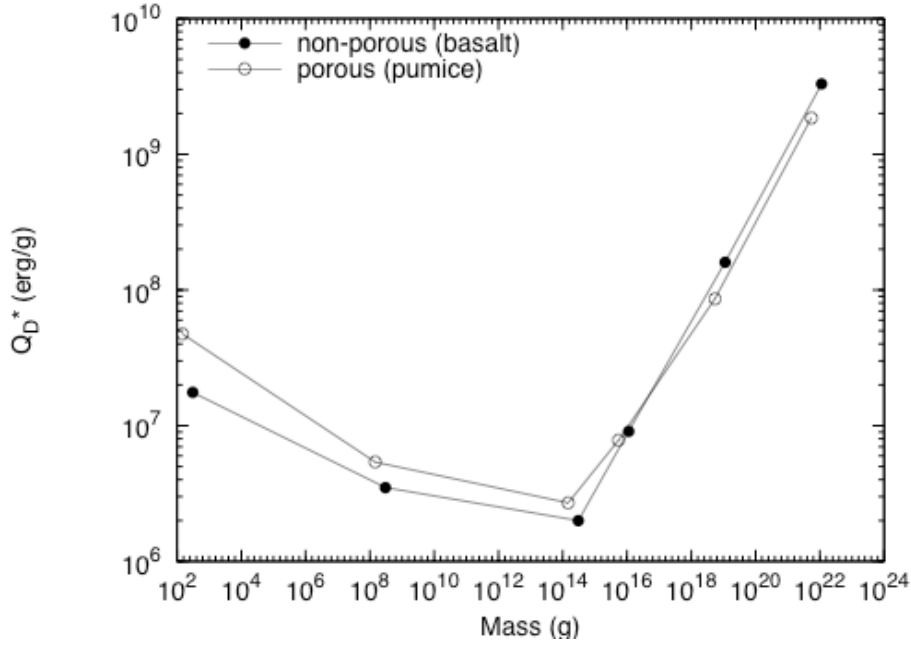


Figure 3: Catastrophic specific impact energy threshold  $Q_D^*$  (erg/g) as a function of the target mass (g). The impact speed and angle are 3 km/s and  $45^\circ$ , respectively. The internal structure of the target is either porous or non-porous, as indicated on the plot.

## V.2. Influence of the impact velocity

The characterization of  $Q_D^*$  for targets of a given size involves both the size and the speed of the projectile. For a given impact speed, the projectile's size is varied, which is what was done to produce Figs. 2 and 3. It is also important to determine the dependency of  $Q_D^*$  on the impact speed. Figures 4 and 5 show the results for the porous and non-porous targets, respectively, for impact speeds of 3 and 5 km/s. In the porous case,  $Q_D^*$  is systematically higher using higher impact speed. In the non-porous case, we find that for the largest considered target size (100 km),  $Q_D^*$  becomes smaller for the higher impact speed. This change was already apparent in the results by Benz and Asphaug (1999). Stewart and Leinhardt (2008) also noticed that the slope of the  $Q_D^*$  curve at 3 km/s becomes shallower for basalt targets with large sizes and interpreted this behavior as a signature of a larger contribution of the projectile mass as it becomes a significant fraction of the target mass. However, we checked that including the projectile particles in the computation of the gravitational phase of the disruption of our 100 km-radius basalt target at both impact speeds, i.e. 3 km/s and 5 km/s, did not lead to a different outcome, i.e.  $Q_D^*$  and the fragment size distributions are identical, and therefore the explanation of this change must reside elsewhere. To provide results of interest for the deflection of an Apophis-like object, we also characterized  $Q_D^*$  for porous targets of 300 meters in radius using higher projectile speeds (i.e. 7 and 10 km/s, in addition to 3 and 5 km/s) and found that  $Q_D^*$  keeps increasing with the impact speed, which is consistent with the trend proposed by scaling laws (Housen and Holsapple 1990):

$$Q_D^* = C\rho R^{3\mu}V^{-3\mu+2} \quad (2)$$

where  $C$  is a constant,  $\rho$  is the density,  $V$  is the impact velocity,  $R$  is the target radius and  $\mu$  is the so-called coupling parameter. Despite the fact that the considered porous target's radius (300 meters) is close to the transition between the strength and gravity regimes, we can still reasonably fit this scaling relationship, which is only appropriate for the gravity regime, with  $\mu = 0.43 \pm 0.01$  and  $C = 4.6 \pm 0.6 \times 10^{-4}$ . Note that our value of  $\mu$  is consistent with the values found in experiments

involving porous materials (e.g. Housen and Holsapple, 1999b).

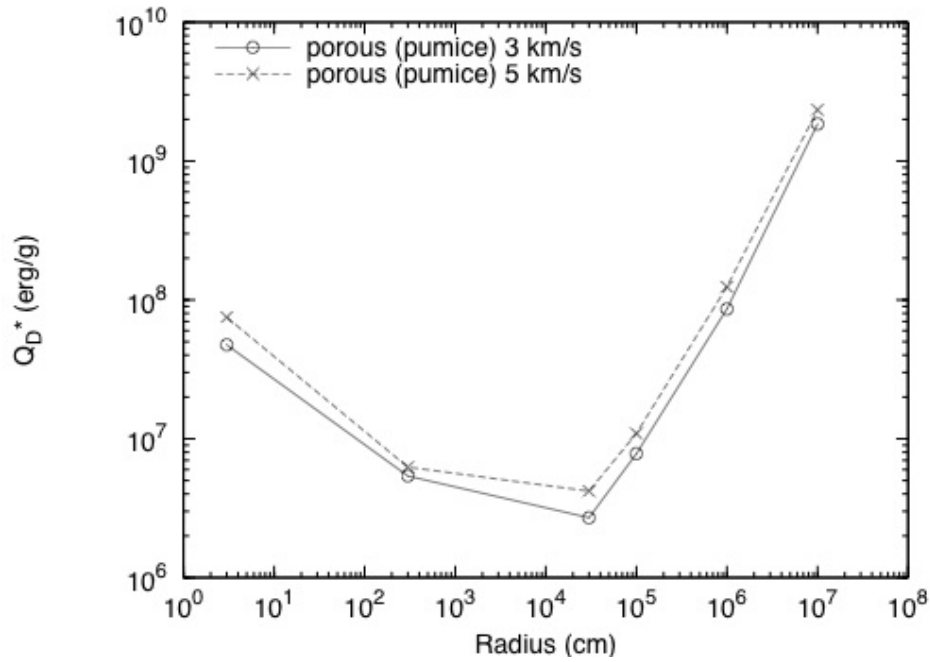


Figure 4: Catastrophic specific impact energy threshold  $Q_D^*$  (erg/g) as a function of porous target radius  $R$  (cm) for impact speeds of 3 and 5 km/s and an impact angle of  $45^\circ$ .

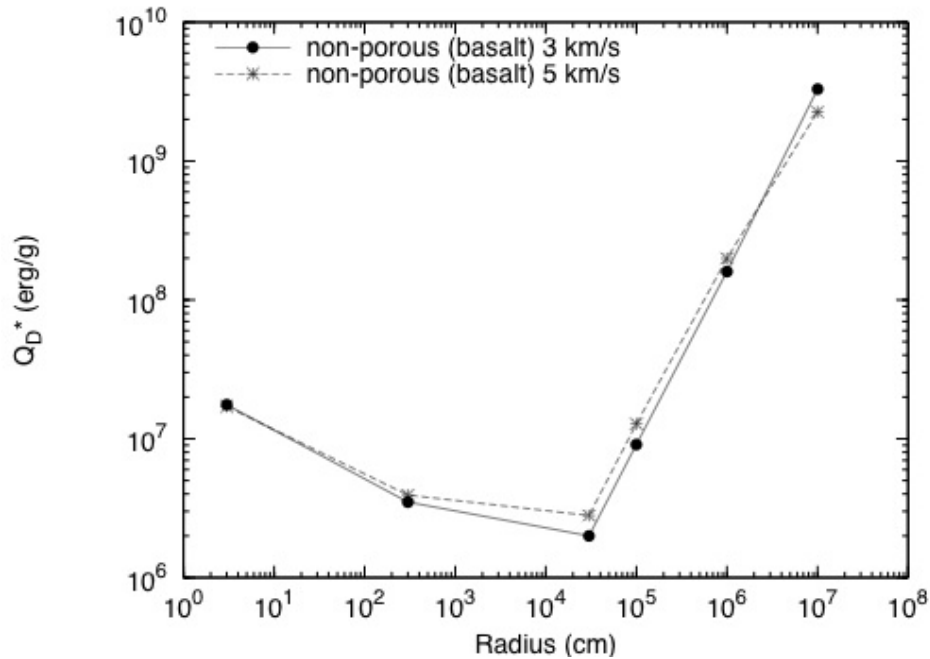


Figure 5: Catastrophic specific impact energy threshold  $Q_D^*$  (erg/g) as a function of non-porous target radius  $R$  (cm) for impact speeds of 3 and 5 km/s and an impact angle of  $45^\circ$ .

### V.3. Power law scaling

For practical use by collisional evolution models, we fit (by eye) the  $Q_D^*$  curves of both kinds of targets, for the impact speeds investigated, by power laws of the form:

$$Q_D^* = Q_0 (R_{pb}/1\text{cm})^{a+B\rho} (R_{pb}/1\text{cm})^b \quad (3)$$

where  $R_{pb}$  is the radius of the parent body,  $\rho$  its density in  $\text{g/cm}^3$  and  $Q_0$ ,  $B$ ,  $a$ ,  $b$  are constants to be determined. Such a functional form is often used in scaling law approaches with the two terms representing the strength and gravity regimes, respectively. Figure 6 shows our fits for the impact speed of 3 km/s. The same kind of qualitative fit is at the origin of the values given in Table 3 for the impact speed of 5 km/s. As it can be seen, we find slightly different slopes for the two materials and the two impact speeds, respectively.

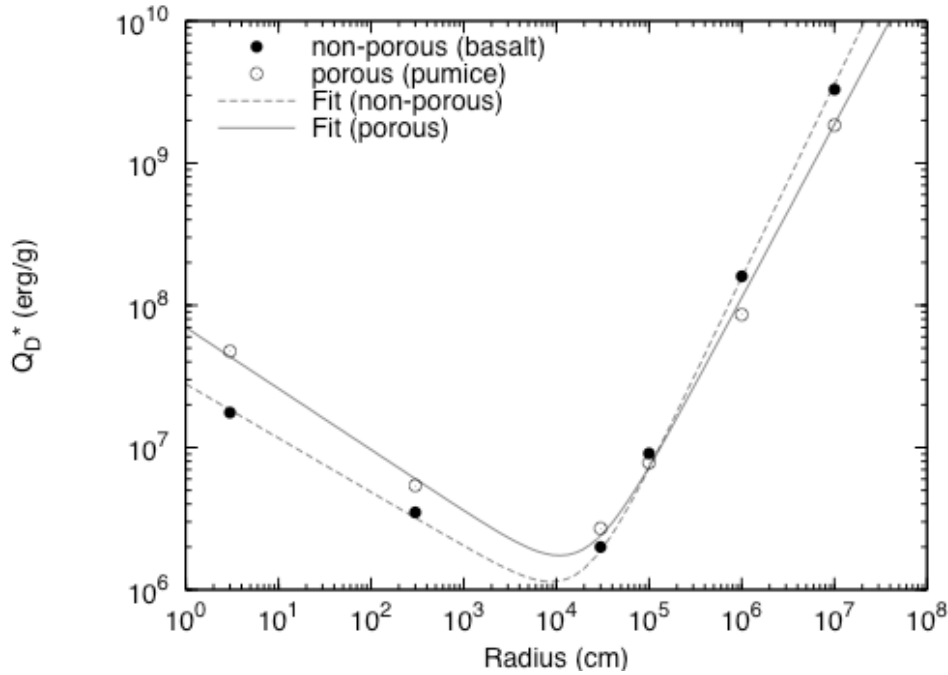


Figure 6: Fits of the catastrophic specific impact energy threshold  $Q_D^*$  (erg/g) as a function of target radius  $R$  (cm) using power laws. The impact speed is 3 km/s and the impact angle is  $45^\circ$ .

Material	$V_{\text{impact}}$ (km/s)	$Q_0$ (erg/g)	$B$ (erg $\text{cm}^3/\text{g}^2$ )	$a$	$b$
Porous (pumice)	3	$7.0 \times 10^7$	4.15	-0.43	1.22
Porous (pumice)	5	$1.0 \times 10^8$	5.70	-0.45	1.22
Non-porous (basalt)	3	$2.8 \times 10^7$	0.40	-0.38	1.36
Non-porous (basalt)	5	$2.9 \times 10^7$	1.50	-0.35	1.29

Table 3: Fit constants for  $Q_D^*$  (see text for details).

#### V.4. Influence of the tensile and shear strengths

The populations of asteroids and comets are certainly composed of a wide diversity of bodies and therefore, the parameter space of their potential material properties is probably huge. In this section, we investigate the effect of the tensile and shear strengths on the impact response of our non-porous and porous targets. To do so, we model our targets using basalt parameters for non-porous ones and pumice parameters for porous ones, but we decrease the strengths from the nominal values (Table 1) in the first case, and increase them in the second case. The new values of tensile and shear strengths are indicated in Table 4 and we define the corresponding targets as weak non-porous and strong porous targets.

	Weak Non-Porous	Strong Porous
m	9.5	9.5
k	$8.0 \times 10^{37}$	$3.0 \times 10^{28}$
Y	$1.0 \times 10^8$	$3.5 \times 10^{10}$
$\sigma_T(3 \text{ cm})$	$3.3 \times 10^7$	$3.5 \times 10^8$

*Table 4: Same as Table 1 for the weak non-porous and strong porous targets. Note that although the Weibull parameters of the weak non-porous targets are the same as the nominal ones of porous targets, the value of  $\sigma_T(3\text{cm})$  is slightly different; the reason is that the density of non-porous targets (and therefore the volume) is higher than the density of porous ones for a similar diameter.*

As can be seen on Fig. 7, in the strength regime, the strong porous target is much more difficult to disrupt than the nominal non-porous one with identical tensile strength. On the other hand the weak non-porous target is much easier to disrupt than the nominal porous target that has again the same tensile strength. Therefore for the strength values investigated, non-porous targets are easier to disrupt in the strength regime, and the corresponding values of  $Q_D^*$  can differ by several orders of magnitude. Moreover, non-porous weak targets enter in the gravity regime at smaller sizes than their nominal counterparts, as indicated by the earlier change of slope to a positive value of the  $Q_D^*$  curve. The reason is that for a low enough strength, gravity starts dominating at a smaller size. Conversely, the slope of the  $Q_D^*$  curve takes a positive value at larger sizes for the porous strong targets, because when the strength is high, gravity starts influencing the outcome when the size of the target is large enough to compensate from the high strength.

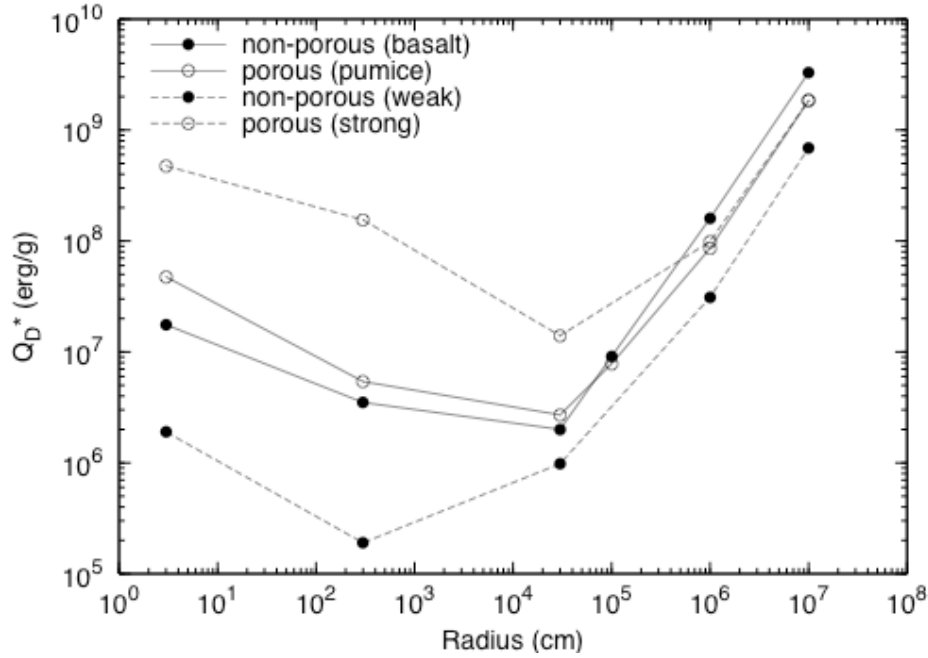


Figure 7: Catastrophic impact energy threshold  $Q_D^*$  (erg/g) as a function of target radius  $R$  (cm) for impact speed of 3 km/s and an impact angle of  $45^\circ$ . Targets are represented by basalt or pumice materials. The label *weak* is used for basalt non-porous targets whose tensile and shear strengths have been decreased from their nominal values, while the label *strong* is used for pumice porous targets whose tensile and shear strengths have been increased from their nominal values (see Tables 1 and 4).

In the gravity regime, the dependency on strength is less dramatic, specially in the porous case for which the effect of strength is almost meaningless. In the non-porous case, the weak target is much easier to disrupt than the nominal case, in agreement with the results of Leinhardt and Stewart (2008). Moreover, the values of  $Q_D^*$  for these weak non-porous targets become smaller than for porous ones. Therefore, one cannot say that a porous target is either systematically easier or more difficult to disrupt than a non-porous one, as it depends on its strength properties and not only on porosity. These results are obviously not ideal for the definition of appropriate deflection strategy solely based on remote data regarding the properties of the threatening object or even on mass and bulk density determination. Indeed, such data are not sufficient to characterize the strength properties of the object. We can only make sure that a disruption can be avoided by to the kinetic impactor an impact energy that is lower than the minimum value of  $Q_D^*$  determined over a reasonable range of strength and material properties.

## VI. Outcome properties for a non-porous parent body

In this section, we analyze the outcome properties from the disruptions of our nominal non-porous targets corresponding to the impact conditions described in Table 2. Here, we concentrate on the gravity regime only, during which re-accumulations can occur. Although the ratios of the largest remnant to the target mass obtained from our simulations do not exactly equal 0.5, they remain close enough to this value that we can reasonably assume that the outcome properties are still a good representation of what would occur at exactly  $Q_D^*$ . Our aim is to determine whether simple rules can be derived from the analysis of these outcome properties that could be easily implemented in a collisional evolution code or a study of deflection strategy. Here, we limit these properties to the fragment size and ejection velocity distributions. Figure 8 shows the fragment size distributions obtained from the disruption of non-porous targets with different diameters. Fragment sizes are

normalized by target diameters to allow a direct comparison. For all the considered target's diameters, the resulting distributions look very similar. This is a practical feature for implementation in a collisional evolution model.

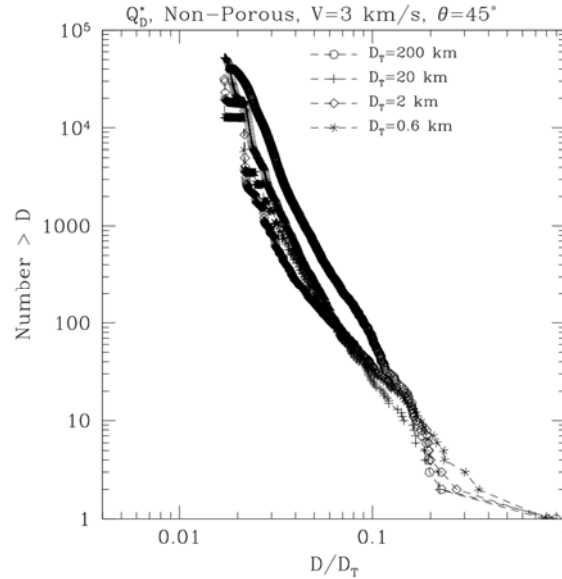


Figure 8: Cumulative diameter (km) distributions of the fragments of simulations at  $Q_D^*$  with an impact speed  $V$  of 3 km/s and an angle of impact  $\theta$  of  $45^\circ$ . The targets are non-porous and their sizes (diameter  $D_T$ ) are indicated on the plot. The fragments' diameters  $D$  are normalized to that of the target  $D_T$ , for a direct comparison.

We also compared the fragment size distribution from a disruption at  $Q_D^*$  using two different impact speeds. As shown on Fig. 9, there is no large sensitivity on the impact speed, at least in the considered range.

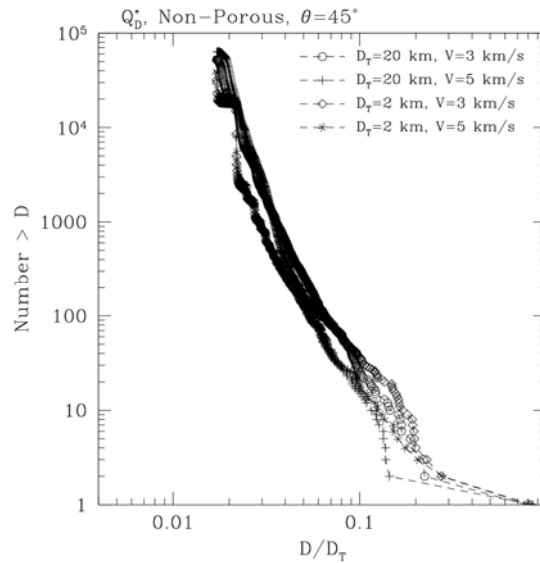


Figure 9: Cumulative diameter (km) distributions of the fragments of simulations at  $Q_D^*$  with an impact speed  $V$  of either 3 km/s or 5 km/s, and an angle of impact  $\theta$  of  $45^\circ$ . The targets are non-porous and their sizes (diameter  $D_T$ ) are indicated on the plot. The fragments' diameters  $D$  are normalized to that of the target  $D_T$ , for a direct comparison.

Therefore, in a collisional evolution model or a study of deflection strategy using a kinetic impactor, it can be reasonably assumed that both the shape and slope of the fragment size distribution from the disruption of a non-porous target at  $Q_D^*$  do not depend on the target's diameter and impact speed, and thus can take one single form. For practical use by collisional evolution models, it is thus possible to characterize a reasonable fit of the fragment size distribution that is valid for all target diameters by a single power law of the form  $N(> D) \propto D^\alpha$  where  $N(> D)$  is the number of fragments with diameter greater than  $D$  and  $\alpha$  is the power-law exponent. Figure 10 shows such a fit for a target of 1 km radius. We find that a value of the power-law exponent in the range between  $-2.2$  and  $-2.7$  can be considered to reasonably fit the size distributions for all the considered target diameters.

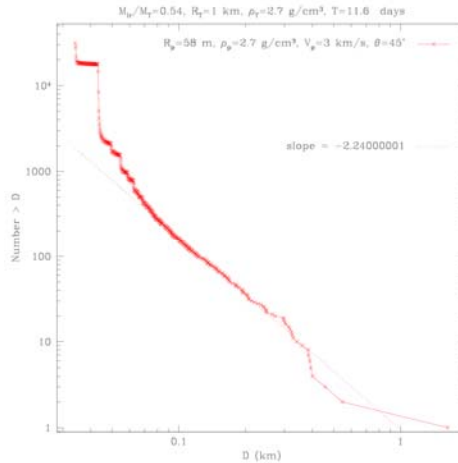


Figure 10: Cumulative diameter (km) distributions of the fragments of the simulation of disruption of the 2 km-size non-porous target at  $Q_D^*$  with an impact speed  $V_p$  of 3 km/s and an angle of impact  $\theta$  of  $45^\circ$ . A reasonable fit to this distribution with a single slope is indicated on the plot.

The analysis of the fragment ejection speeds, and in particular the average, median and largest remnant speeds, show that their values scale with the target diameter (see Fig. 11). A linear fit applies to the relationship between either the average or median speeds and the target diameter in the entire diameter range represented in a log-log plot.

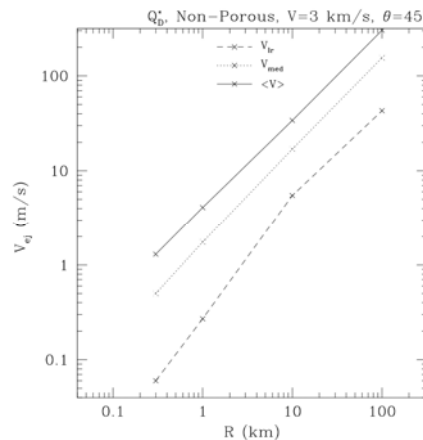


Figure 11: Different fragment ejection speeds as function of the radius  $R$  of non-porous

targets, disrupted at  $Q_D^*$  with an impact speed  $V$  of 3 km/s and an impact angle  $\theta$  of  $45^\circ$ .  $V_{lr}$  stands for the largest remnant's speed, while  $V_{med}$  and  $\langle V \rangle$  are the median and average fragments' speeds, respectively.

Another interesting property is the relationship between fragment speed and mass (Fig. 12). The same result as obtained by Michel et al. (2004a) in a different impact energy regime is found here, i.e. smaller fragments tend to have greater ejection speeds than larger ones. However, there is still a wide spread of values for fragments of a given mass, which makes it difficult to define a power-law relationship between fragment masses and speeds, such as the ones often used in collisional evolution models (see e.g., Davis et al. 2003).

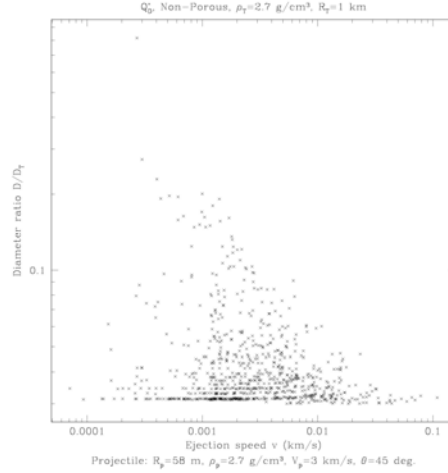


Figure 12: Fragment's diameter  $D$  (normalized to that of the parent body  $D_T$ ) vs. ejection speed obtained from the breakup at  $Q_D^*$  of a non-porous target, 1 km in radius. The impact speed  $V_p$  is 3 km/s and the impact angle is  $\theta = 45^\circ$ . Only fragments with size above the resolution limit (i.e. those that underwent at least one re-accumulation event) are shown here.

## VII. Outcome properties for a porous parent body

The same simulations were performed using our nominal porous targets. The impact conditions are given in Table 2. For all the considered target diameters, the resulting size distributions look very similar (see Fig. 13). On this plot, all the distributions essentially overlap with each other, except in a small range of sizes ( $0.1 < D/D_T < 0.3$ ). Thus, as we did for non-porous targets, for practical use by collisional evolution models, we characterized a reasonable fit of the fragment size distributions that is valid for all target diameters with a single power law.

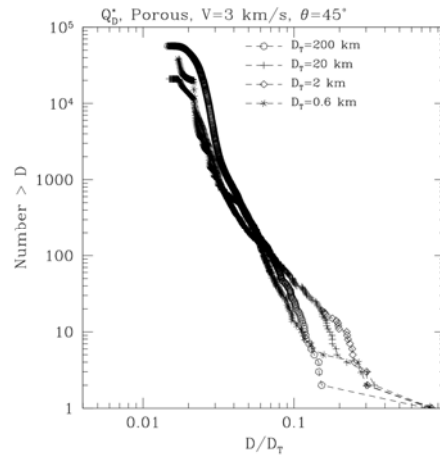


Figure 13: Same as Figure 8 for porous parent bodies.

Figure 14 shows such a fit for the target that is 1 km in radius. We find a best-fit value of the power-law exponent in the same range as for the non-porous case, between about  $-2.2$  and  $-2.7$ , that can be considered to reasonably describe the size distributions for all the considered target diameters. We also characterized the fragment size distribution from a disruption at  $Q_D^*$  of a porous targets of 300 m in radius (Apothis-like size) using four different impact speeds.

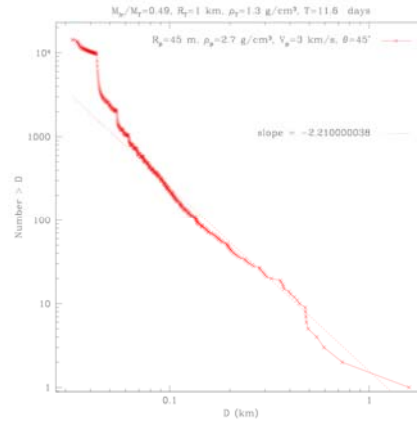


Figure 14: Cumulative diameter (km) distributions of the fragments of the simulation of disruption of the 2 km-size porous target at  $Q_D^*$  with an impact speed  $V_p$  of 3 km/s and an angle of impact  $\theta$  of  $45^\circ$ . A reasonable fit of this distribution with a single slope is indicated on the plot.

As shown in Fig. 15, we find again that there is no large sensitivity on the impact speed, except for the highest one (10 km/s), which shows some discrepancy in the diameter range between about 0.04 km and 0.2 km. Whether this is meaningful or not will require a deeper investigation of the process at such high speeds, which we leave for future studies.

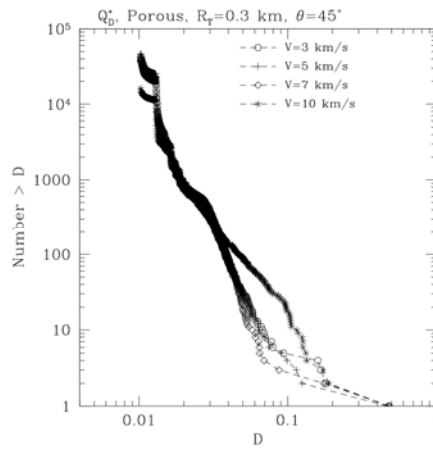


Figure 15: Cumulative diameter (km) distributions of the fragments of simulations at  $Q_D^*$  with an impact speed  $V$  of 3, 5, 7 or 10 km/s, and an angle of impact  $\theta$  of  $45^\circ$ . The targets are porous and 300 m in radius (Aphesis-like size).

Concerning the ejection speeds, the average, median and largest remnant speeds increase with increasing target diameter (see Fig. 16).

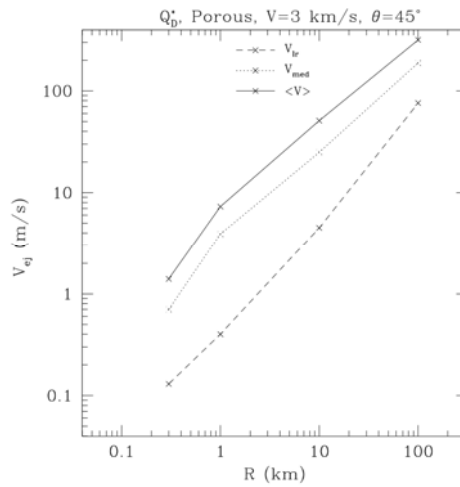


Figure 16: Same as Fig. 11 for the case of porous targets.

As shown in Fig. 17, a wide spread of ejection speeds of fragments of a given mass exists. Consequently it is again difficult to define a power-law relationship between fragment masses and speeds.

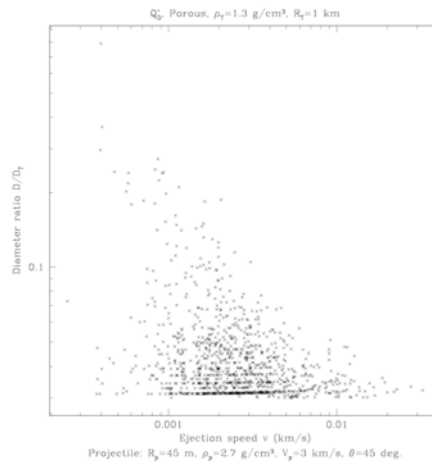


Figure 17: Fragment's diameter  $D$  (normalized to that of the parent body  $D_T$ ) vs. ejection speed obtained from the breakup at  $Q_D^*$  of a porous target, 1 km in radius. The impact speed  $V_p$  is 3 km/s and the impact angle is  $\theta = 45^\circ$ . Only fragments with size above the resolution limit (i.e. those that underwent at least one re-accumulation event) are shown here.

## VIII. Comparison between the outcomes for non-porous and porous targets

The analysis of the outcome properties from the disruption of non-porous and porous targets has allowed us in each case to identify some systematic behaviors, which are either independent of target's size and impact speed (e.g. fragment size distribution) or scale with the target's size (e.g. median and average ejection speeds). In this section, we analyze the systematic differences that can be identified and that are due to the different internal structures of the parent body. Note that we consider again only the gravity regime.

### VIII.1. Fragment size distribution

For a given internal structure, the shape of the fragment size distribution certainly depends on the impact energy regime. For instance, in the case of a monolithic non-porous parent body, higher impact energies lead to a more continuous fragment size distribution (Michel et al. 2001, 2002, Durda et al. 2007). Moreover, Michel et al. (2003) found that the fragment size distribution from the disruption of pre-shattered non-porous targets tends to be more continuous than those from the disruption of monolithic non-porous targets, for all considered target diameters. Obviously, the parameter space could not be covered exhaustively, so it cannot be guaranteed that these conclusions can be generalized. Here, at impact energies close or equal to  $Q_D^*$ , we actually find that there is not much difference between the size distributions obtained from either a non-porous target or a porous one, at least for the two materials considered (basalt and pumice). For instance, Fig. 18 shows similar size distributions obtained from the disruption of 1 km-radius porous and non-porous targets. As we indicated in previous sections, the power-law exponent that can be used to fit the size distributions is in the same range for both kinds of targets.

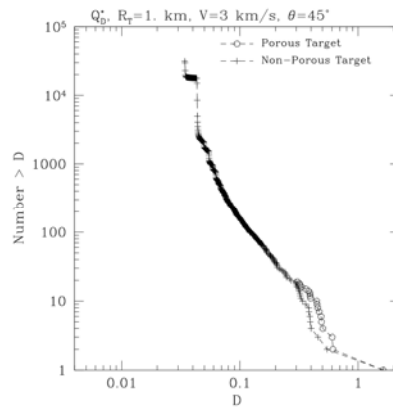


Figure 18: Comparison between the size distributions obtained from the disruption of 1 km-radius porous and non-porous targets with an impact speed  $V$  of 3 km/s and an impact angle  $\theta$  of  $45^\circ$ .

### VIII.2. Ejection speeds

The average and median speeds are slightly higher for the porous targets than for the non-porous ones. This can be seen in Table 5 and in Figs. 19 and 20. As discussed in Section V.1, this (counter intuitive) result can probably be explained by the higher density and strength of the non-porous material. Note that these comparisons are made from simulations leading to values of  $M_{lr}/M_{pb}$  that are not exactly the same in all cases, so small differences must be interpreted with caution. Hence, we can reasonably conclude that average and median speeds are of the same order in general for both kinds of target's internal structure, although there is a systematic trend toward higher values for the porous targets. To easily implement these results in a collisional evolution model, one can assume that the largest remnant, average and median ejection speeds scale with the target's diameter. Then, slightly greater values can be assigned to fragments from porous targets.

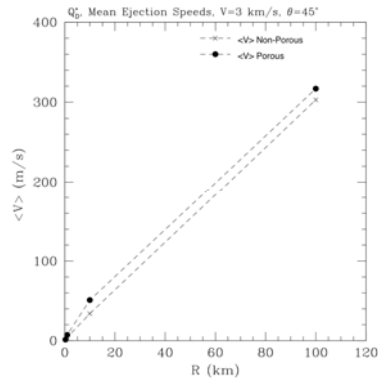


Figure 19: Mean ejection speed  $\langle V \rangle$  as a function of target radius  $R$ . The impact speed  $V$  is 3 km/s and the impact angle  $\theta$  is  $45^\circ$ . The results from the two kinds of target's internal structure are shown, as indicated on the plot.

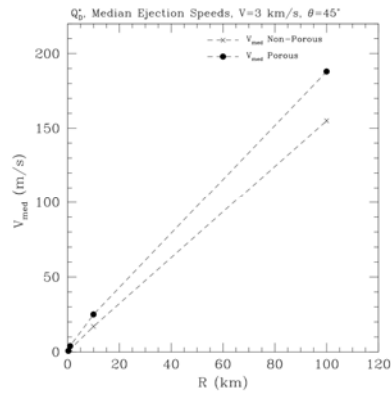


Figure 20: Median ejection speed  $V_{med}$  as a function of target radius  $R$ . The impact speed  $V$  is 3 km/s and the impact angle  $\theta$  is  $45^\circ$ . The results from the two kinds of target's internal structure are shown, as indicated on the plot.

## IX. Conclusions

In this report, we presented the results of complete simulations of disruptions that allowed the determination of the relationships between the specific impact energy threshold for disruption, called  $Q_D^*$ , and both the target diameter and its internal structure represented by porous and non-porous materials made of pumice and basalt. We confirmed the results from previous studies indicating that  $Q_D^*$  first decreases with target size in the strength regime and then increases with target size in the gravity regime. Moreover, we found that a porous body (as defined by our nominal model) requires more energy to be disrupted than its non-porous counterpart in the strength regime. In the gravity regime, the situation is reversed but the difference remains small. This might explain why, to first order, collisional evolution models could get away with only a single scaling law to reproduce the main characteristics of the asteroid populations (e.g. Bottke et al. 2005), despite the wide variety of internal properties that they can have. However, by changing the nominal values of the tensile and in particular the shear strength of our targets, we found that in the gravity regime, the value of  $Q_D^*$  is not greatly influenced by the assumed strength for porous targets. Conversely, in the case of non-porous targets, the value of  $Q_D^*$  decreases significantly with decreasing strength. Therefore, in the gravity regime one cannot reasonably assume systematically that porous targets are easier or more difficult to disrupt than non-porous ones, as it depends on the assumed strengths of the latter. We plan to investigate the effect of other material properties as well as other kinds of materials in the future. The value of  $Q_D^*$  also depends on the impact velocity and we find similar tendency as previous studies, namely an increase of  $Q_D^*$  with the impact speed. We then propose a scaling with speed for our porous targets, and find that it requires parameters that are consistent with what is expected for porous materials.

We next determined the outcome properties of the disruptions at  $Q_D^*$ , limited here to the fragment size and ejection velocity distributions in the gravity regime. We found that the size distributions keep the same qualitative aspect independent of the parent body's size and impact speed in the investigated range. For both porous and non-porous parent bodies, they can be represented by a power-law whose exponent can be used to approximate the distributions produced from all target's sizes. The average and median ejection speeds show also some systematic trends, i.e. they increase systematically with the target's diameter. Moreover, they are of the same order for both kinds of parent bodies, although slightly higher in the porous case. These results (although limited to a particular specific impact energy) can be easily implemented in numerical algorithms aimed at studying the collisional evolutions of small body populations, or at defining the maximum impact energy that leads to a deflection (instead of a disruption) and the resulting ejecta properties. They provide systematic trends in the outcome properties and scaling laws for  $Q_D^*$ , at least for the two

kinds of target internal structure that we investigated, using nominal values of their material properties. Obviously, the real internal structures of small bodies cannot be limited to these two models and we plan to develop other models and use different material properties in order to study their resistance as well as the outcome properties of their disruption. While we limited our study to monolithic bodies, pre-shattered bodies and rubble piles, which may contain macroscopic voids and/or some microporosity, are likely to be present in the asteroid population. It is then essential to understand how macroscopic voids alone or combined with microporous properties as considered in this paper can influence the critical specific impact energy for disruption and whether they show some signature in the outcome properties. Then, using an improved version of our N-body code (Richardson et al. 2009), we shall also be able to characterize the spin and shape distributions of fragments, in addition to the size and velocity distributions. It is already clear that a deep understanding of collisions between small bodies requires the investigation of a huge parameter space. As a conclusion, there is room for a great number of studies in order to characterize the impact energies and outcome properties that will allow us to provide to collisional evolution models the different recipes that are valid for all impact conditions and kinds of real small bodies. Furthermore, this information is crucial to assess the efficiency of mitigation techniques aimed at deflecting a potential impactor with the Earth, as a first step requires a characterization of which impact conditions prevent the disruption of the body and rather permit its deflection.

## **X. References**

- Ahrens, T.J., Harris, A.W., 1992. Deflection and fragmentation of near-Earth asteroids. *Nature* 360, 429-433.
- Asphaug, E., Ryan, E.V., Zuber, M.T., 2002. Asteroid interiors. In: Bottke, W.F., Cellino, A., Paolicchi, P., Binzel, R.P. (Eds.), *Asteroids III*. Univ. of Arizona Press, Tucson, pp. 463-484.
- Benz, W., 1990. Smooth particle hydrodynamics: A review. In *Numerical Modeling of Nonlinear Stellar Pulsations. Problems and Prospects* (J. R. Buchler, Ed.), pp. 269–288. Kluwer Academic, Dordrecht.
- Benz, W., Asphaug, E., 1994. Impact simulations with fracture. I. Method and tests. *Icarus* 107, 98-116.
- Benz, W., and Asphaug, E., 1995. Simulations of brittle solids using smooth particle hydrodynamics. *Computer Physics Communications* 87, 253.
- Benz, W., and Asphaug, E., 1999. Catastrophic Disruptions Revisited. *Icarus* 192, 5-20.
- Bottke, W.F., Durda, D.D., Nesvorny, D., Jedicke, R., Morbidelli, A., Vokrouhlicky, D., and Levison, H. 2005. The fossilized size distribution of the main asteroid belt. *Icarus* 175, 111.
- Britt D.T., and Consolmagno G.J. 2000. The porosity of dark meteorites and the structure of low-albedo asteroids, *Icarus* 146, 213-219.
- Carusi, A., Valsecchi, G.B., D'Abramo, G., Boattini, A., 2002. Deflecting NEOs in route of collision with the Earth. *Icarus* 159, 417-422.
- Carroll, M.M., Holt, A.C., 1972. Suggested modification of the P - ! model for porous materials. *J. Appl. Phys.* 43, 759-761.
- Davis, D. R. 2003. The experimental and theoretical basis for studying collisional disruption in the

solar system. *Impacts on Earth*, 113.

Durda, D.D., Bottke, W.F., Nesvorny, D., Enke, B. L., Merline, W. J., Asphaug, E., Richardson, D. C., 2007. Size-frequency distributions of fragments from SPH/N-body simulations of asteroid impacts: Comparison with observed asteroid families. *Icarus* 186, 498.

Giorgini, J.D., Benner, L.A.M., Ostro, S.J., Nolan, M.C., Busch, M.W., 2008. Predicting the Earth encounters of (99942) Apophis. *Icarus* 193, 1-19.

Grady, D.E., Kipp, M.E., 1980. Continuum modelling of explosive fracture in oil shale. *Int. J. Rock Mech. Min. Sci. & Geomech. Abstr.* 17, 147–157.

Herrmann, W., 1969. Constitutive equation for the dynamic compaction of ductile porous materials. *J. Appl. Phys.*, 40, 2490-2499.

Holsapple, K.A., Gibling, I., Housen, K., Nakamura, A., Ryan, E., 2002. Asteroid impacts: Laboratory experiments and scaling laws. In: Bottke, W.F., Cellino, A., Paolicchi, P., Binzel, R.P. (Eds.), *Asteroids III*. Univ. of Arizona Press, Tucson, pp. 443.

Housen, K. R., and Holsapple, K. A., 1990. On the fragmentation of asteroids and planetary satellites. *Icarus* 84, 226-53.

Housen, K. R., Holsapple, K. A., Voss, M. E., 1999a. Compaction as the origin of the unusual craters on the asteroid mathilde. *Nature* 402, 155157.

Housen, K. R., Holsapple, K. A., 1999b. Scale Effects in Strength-Dominated Collisions of Rocky Asteroids, *Icarus*, 142, pp. 21

Jutzi, M., Benz, W., Michel, P., 2008. Numerical simulations of impacts involving porous bodies. I. Implementing sub-resolution porosity in a 3D SPH hydrocode. *Icarus* 198, 242-255.

Jutzi, M., Michel, P., Hiraoka, K., Nakamura, A. M., Benz W., 2009a. Numerical simulations of impacts involving porous bodies: II. Comparison with laboratory experiments. *Icarus*, 201, 802-813.

Jutzi, M., Michel, P., Benz, W., Richardson, D.C., 2009b. The formation of the Baptistina family by catastrophic disruption: porous versus non-porous parent body. *MAPS*, accepted.

Jutzi, M., Michel, P., Benz, W., 2009c. Numerical simulations of impact deflections: influence of the target's internal structure. *Proceedings of the 1<sup>st</sup> AAI Planetary Defense Conference, Grenada (Spain)*.

Leinhardt, Z. M., Stewart, S.T., 2008. Full numerical simulations of catastrophic small body collisions. *Icarus* 199, 542-559.

Libersky, L.D., Petschek, A.G., 1991. Smooth Particle Hydrodynamics with strength of materials. In: Trease, Fritts, Crowley (Eds.), *Proc. Next Free-Lagrange Method, Lecture Notes in Physics 395*, Springer-Verlag, Berlin, pp. 248-257.

McGlaun, J. 1990. CTH - a three dimensional shock physics code. *Int. J. Impact Eng* 10.

Michel, P., Benz, W., Tanga, P., Richardson, D.C., 2001. Collisions and gravitational reaccumulation: Forming asteroid families and satellites. *Science* 294, 1696-1700.

- Michel, P., Tanga, P., Benz, W., Richardson, D.C., 2002. Formation of asteroid families by catastrophic disruption: Simulations with fragmentation and gravitational reaccumulation. *Icarus* 160, 10-23.
- Michel, P., Benz, W., Richardson, D.C., 2003. Disruption of fragmented parent bodies as the origin of asteroid families. *Nature* 421, 608-611.
- Michel, P., Benz, W., Richardson, D.C., 2004a. Catastrophic disruption of pre-shattered parent bodies. *Icarus* 168, 420-432.
- Michel, P., Benz, W., Richardson, D.C., 2004b. Catastrophic disruption of asteroids and family formation: a review of numerical simulations including both fragmentation and gravitational reaccumulations. *PSS* 52, 1109-1117.
- Michel, P., Jutzi, M., Benz, W., 2009. Catastrophic Impact Energy Threshold for Disruption of Small Porous and Non-Porous Asteroids: a Crucial Information for Deflection Strategies. *Proceedings of the 1<sup>st</sup> AAI Planetary Defense Conference, Grenada (Spain)*.
- Monaghan, J.J., 1992. Smooth particle hydrodynamics. *Ann. Rev. Astron. Astrophys.* 30, 543–574.
- Nakamura, A.M.; Fujiwara, A., 1991. Velocity distribution of fragments formed in a simulated collisional disruption. *Icarus* 92, 132-146.
- Richardson, D.C., 1994. Tree Code Simulations of Planetary Rings. *MNRAS* 269, 493-511.
- Richardson, D. C., Quinn, T., Stadel, J., Lake, G., 2000. Direct large-scale N-body simulations of planetesimal dynamics. *Icarus* 143, 45-59.
- Richardson D.C., Michel P., Walsh, K.J. and K.W. Flynn 2009. Numerical simulations of asteroids modelled as gravitational aggregates with cohesion. *Planetary and Space Science* 57, 183-192.
- Saha, P., Tremaine, S., 1992. Symplectic integrators for solar system dynamics. *Astron. J.* 104, 1633-1640.
- Stadel, J., 2001. Cosmological N-body simulations and their analysis. Thesis, University of Washington, Seattle, 126pp.
- Tillotson, J.H., 1962. Metallic equations of state for hypervelocity impact. General Atomic Report GA-3216, July 1962.
- Wilkison, S.L., Robinson, M.S., Thomas, P.C., Veverka, J., McCoy, T.J., Murchie, S.L., Prockter, L.M., Yeomans, D.K., 2002. An estimate of cross porosity and implications for internal structure. *Icarus* 155, 94-103.
- Yeomans, D.K., et al., 1997. Estimating the mass of asteroid 253 Mathilde from tracking data during the NEAR flyby. *Science* 278, 2106-2109.